Title: Theta coordinates hippocampal-entorhinal ensembles during wake and rest

Authors: Diogo Santos-Pata[1], Caswell Barry[2] & H. Freyja Olafsdottir[2,3*]

Affiliations:

1. Institute for Bioengineering of Catalonia, Barcelona, Spain

2. Department of Cell and Developmental Biology, University College London, London, UK.

3. Donders Institute for Brain, Cognition & Behaviour, Radboud Universititeit, Nijmegen, the Netherlands.

*Corresponding author. Email: freyja.olafsdottir@donders.ru.nl

Abstract: Precisely timed interactions between hippocampal and cortical cells, during quiescent periods dominated by replay of CA1 cell sequences, are thought to support memory consolidation. However, the processes during encoding that lead to coordinated offline replay remain poorly understood. We found entrainment of deep-layer medial entorhinal cortex (dMEC) cells to CA1 cell assemblies dictated their later recruitment and synchronisation with hippocampal replay. These assembly-entrained cells participated preferentially in replay which included their CA1 assembly partner and in forward-projecting replay sequences. Finally, replay coordination of these dMEC cells showed a marked experience-dependent increase; becoming stronger as an animal became fluent with a novel spatial task. Together these findings suggest cell assemblies may support information propagation in hippocampo-cortical circuits and the establishment of long-term memories.

One-Sentence Summary: Entrainment of cortical cells to hippocampal cell assemblies dictates their later involvement in hippocampal replay

Main Text: Reactivation of hippocampal cell sequences ('replay'(1)) during quiescent periods is thought to be the primary mechanism leading to the establishment of long-term memories (i.e 'memory consolidation')(2, 3). Indeed, disrupting replay has been found to impair spatial memory(2, 4) and replay periods are associated with heightened hippocampal-cortical synchrony(5, 6) as well as synergistic replay(7, 8). Importantly, disrupting hippocampal-cortical coordination during replay is known to impair memory consolidation(9). Critically, the processes during encoding that lead to coordinated hippocampal-cortical replay - paving the way for future memory consolidation - are poorly understood.

A wealth of research implicates the hippocampal theta rhythm(10) - a 5-12Hz oscillation, dominating the hippocampal local field potential (LFP) during locomotor activity - in plasticity and memory processes(11-13). Specifically, theta is thought to orchestrate the formation of hippocampal cell assemblies(14, 15) - small networks of neurons, with overlapping firing fields, that become active within ultra-short (10-30ms) time windows and whose activity is confined to particular phases of the theta cycle. Prominent theories suggest cell assemblies represent the fundamental neural code supporting multiple core functions of the brain, including memory formation(11, 16). This is due to the transient lifetime of a cell assembly which makes it an ideal candidate for inducing plasticity (i.e. spike-timing-dependent-plasticity(17)). Thus, we hypothesised that perhaps synergistic hippocampal-cortical replay also depends on the formation of hippocampal-cortical cell assemblies during encoding?

To explore this question we co-recorded CA1 place cells and excitatory cells from the deep layers (V/VI) of the MEC (Figure 1B, Fig. S1) – the main cortical output region of the hippocampus - over 2-6 days while animals ran on a Z-shaped track for food reward (RUN), while they rested following the track session (REST) and during a foraging session in the open-field following REST (Figure 1A, as described previously Olafsdottir et al.(*7*,*8*)). As the identification of replay

trajectories depends on cells displaying spatially confined activity, we limited our analyses to dMEC cells which fell into one of the following functional classes: grid cells(18), head direction cells(19), conjunctive grid and head direction cells(20), border cells (21) and other spatial cells (53.52% of dMEC cells, Fig.1C, see Materials and Methods).

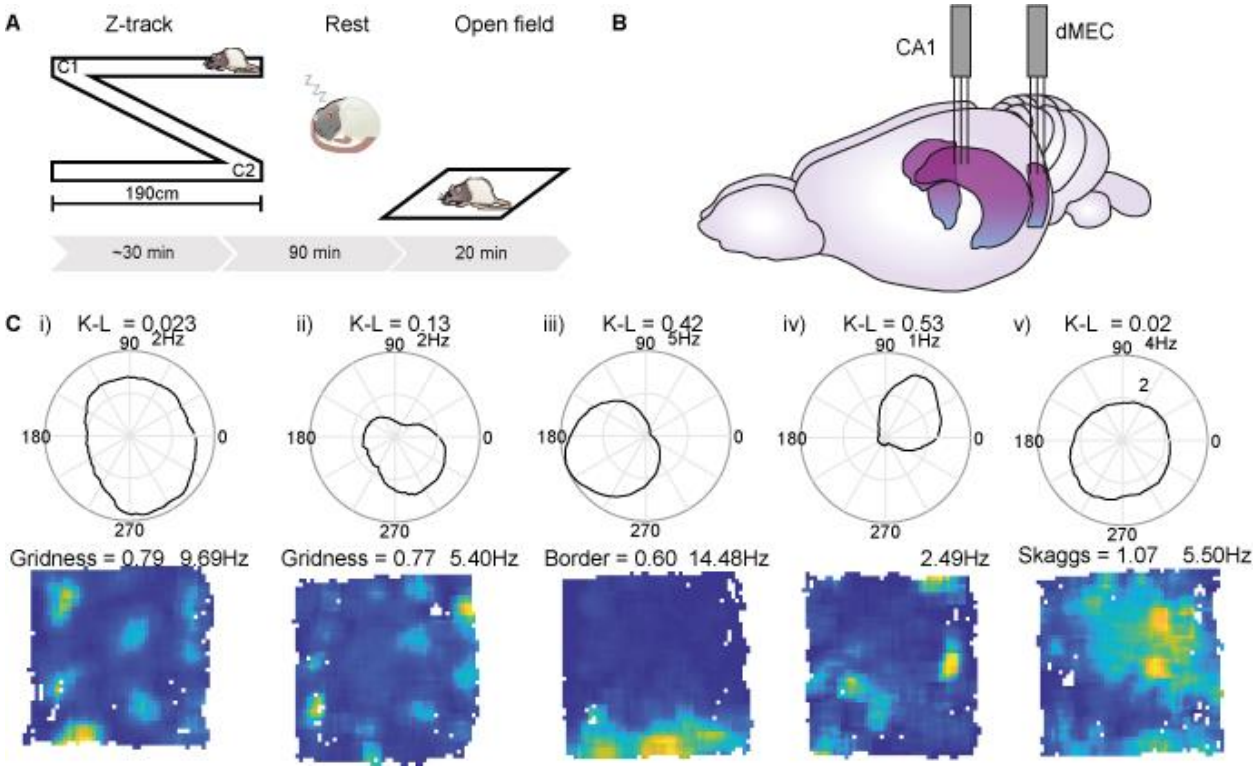

Figure 1. Simultaneous recording of spatial cells from CA1 and dMEC. (**A**) Schematic overview of the study. Rats shuttled back and forth between the ends of a Z-shaped track (left), and then rested for 90min in a separate environment (middle) and then completely a 20min foraging session in the open field. (**B**) Two tetrode arrays were implanted in the CA1 and dMEC. (**C**) Functional cell type recorded in dMEC. Top: polar plot showing direction tuning (title = direction tuning based on K-L divergence). Bottom: ratemaps showing spatial modulation, title on the left shows grid score(20) (far left, middle left), border score (21) (middle) or skaggs information (22) (bits/spike, far right) and the peak rate (Hz, on the right). Spatial cell type from left-right: Grid cell, conjunctive cell, border cell, head direction cell, spatial cell.

We first sought to identify dMEC cells that were entrained by a CA1 cell assembly. Given the role of theta in orchestrating cell assemblies we searched for dMEC cells that were coupled to CA1 cells in the theta-band. Specifically, we constructed cross-correlograms (+/-1sec) of spikes from pairs of dMEC and CA1 cells (Fig. 2A-C). The cross-correlograms were band-passed filtered in the theta- (5-12Hz) and broad-band (20-125Hz) and the ratio between the amplitude in the two bands was computed (i.e. high theta-to-broad-band ratio indicates theta-band coupling, Fig. 2C, see also Materials and Methods). To estimate significance, the dMEC spike train was shifted by random amounts (-2 to 2sec) 100 times. dMEC cells which showed significant coupling to at least one co-recorded CA1 cell in the theta-band were labelled as dMEC assembly cells (Materials and Methods). Using this method we observed a bimodal distribution in the dMEC population (Fig. S2) with just under half the cells showing such assembly-like coupling (40.4%, N=139, Fig. 2D, Fig. S3). Further, consistent with the suggestion that these cells are entrained by CA1 cell assemblies, they showed stronger phase coherence to hippocampal LFP-theta than other dMEC cells (assembly dMEC = 0.27 +/-0.03 other dMEC = 0.34+/-0.02, $p = 0.037$, Fig. 2G). Indeed, assembly cells showed similar phase coherence as co-recorded CA1 cells (0.25 +/-0.01, $p>0.5$), while other dMEC cells showed significantly lower coherence ($p<0.0001$). Finally, assembly cells also showed a preferred firing phase to hippocampal theta more closely aligned with that of CA1 cells than other dMEC cells ($p = 0.01$, Fig. 2H). Importantly, we found the different functional classes were equally represented among the two cell types (all p-values > 0.05, see Fig. S4) and the two groups did not differ in the degree of firing field overlap with co-recorded place cells ($p = 0.13$, Fig. 2E), or theta modulation of the individual spike train ($p=0.18$ Fig. 2F). Among the assembly cells, moreover, field overlap was similar for CA1 assembly cell partners and other CA1 cells ($p = 0.34$), suggesting the observed dMEC theta-band coupling to CA1 cells was not a simple

by-product of theta co-modulation or firing field overlap but may rather reflect genuine entrainment by a CA1 cell assembly.

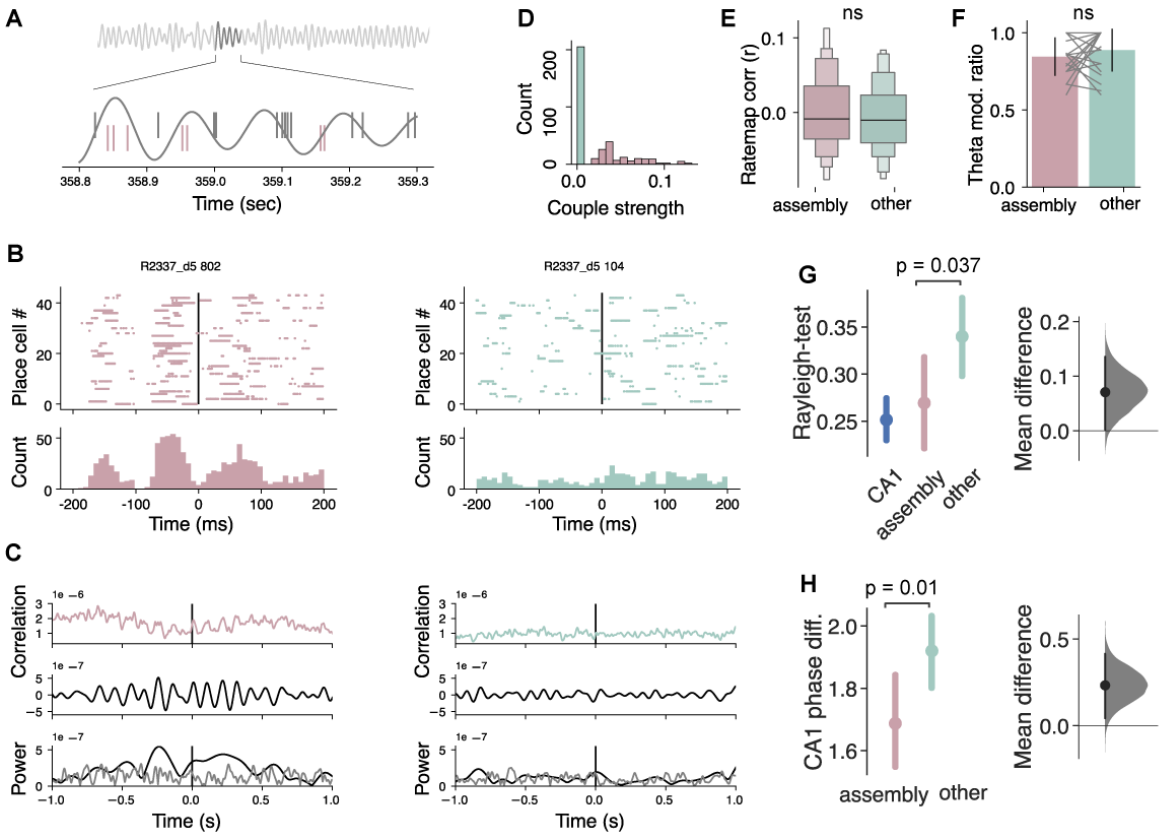

Figure 2. Theta-band synchrony between dMEC and CA1 place cells. (A) Theta synchrony between a CA1 and dMEC cell over 4 oscillatory theta cycles (500ms). Black raster shows CA1 spikes and pink raster dMEC assembly cell spike (**B**) Top: lagged spike synchronization between dMEC and CA1 cells (assembly left and other right). Dots represent time bins (2 ms) where dMEC and CA1 spike cross-correlation surpasses significance. Bottom: distribution of significant spikes per time bin. (**C**) Cross-correlations (top), theta-filtered (middle), and their theta- and broad-band filtered profiles (bottom). The ratio between these two bands was used to measure theta-band coupling. Right and left panels same as B. (**D**) Couple strength scores distribution for assembly and other cell types. Couple strength indexes how many CA1 cells a dMEC cell shows theta-band coupling to. (**E**) Average correlation between dMEC and CA1 ratemaps. (**F**) Ratio of theta

modulated neurons per animal/session. (**G**) Phase coherence to hippocampal theta. (Rayleigh uniformity score). Left: Rayleigh score for CA1, assembly and other cells. Right: Bootstrapped mean difference between assembly and other cells scores. (**H**) Phase preference (radians) similarity between CA1 cells and dMEC assembly and other cells. Right: Bootstrapped mean difference between assembly and other cells.

As cell assemblies have been implicated in memory-related processes, we asked if assembly dMEC cells were preferentially recruited during hippocampal replay events. To address this question, we firstly analysed dMEC activity in the two subpopulations during candidate hippocampal replay events (see Materials and Methods). First, we observed that both assembly dMEC cells as well as other cells were positively modulated by the occurrence of hippocampal replay (Fig. 3A-B), displaying greater activity during replay than periods outside replay. However, assembly dMEC cells showed significantly stronger modulation than other dMEC cells during replay events (Fig. 3B, $p < 0.0001$ at all time bins +/- ~100ms from the middle of a replay event). Moreover, we found assembly dMEC cells were active in on average 8.54% (SD = 7.52) of replay events while other dMEC cells were on average active in 6.51% (SD = 5.42) of replay events, a difference found to be statistically significant ($p = 0.0019$, Fig. 3C).

Further, to assess if dMEC cells displaying assembly-like coupling to CA1 cells were also more functionally coordinated with hippocampal replay, we identified candidate replay events that expressed linear trajectories and assessed if the activity of the assembly dMEC cells was consistent with the trajectories encoded by CA1 cells (Fig. 3D , see Materials and Methods and Olafsdottir et al.(*7*),). To determine if the obtained replay coordination exceeded chance levels we randomly permuted the cell ID of dMEC cells 100 times. To note, similar results were obtained when the

spatial location of dMEC firing fields were shuffled (see Fig. S5). We found both assembly dMEC as well as other dMEC cells showed significant coordination with hippocampal replay events, expressing more similar locations to CA1 cells during replay than expected by chance (assembly dMEC cells: $p < 0.0001$, other cells: $p = 0.0001$ Fig. 3E,F). However, dMEC assembly cells showed significantly greater coordination with hippocampal replay compared to dMEC cells which did not show assembly-like coupling ($p < 0.0001$, Fig. 3G). Yet, hippocampal replay can either express place cell sequences in the order experienced ('forward' replay) or depict backward-projecting sequences ('reverse' replay). Importantly, *forward* replay is thought to be more favourable for memory consolidation(3). Thus, we asked is dMEC assembly cell coordination with replay heightened for forward events? To address this question we analysed the coordination of assembly and other dMEC cells with hippocampal replay separately for forward and reverse events. We found dMEC assembly cells showed significant coordination with both forward and reverse replay (forward: $p < 0.0001$, reverse: $p = 0.0066$, Fig. 4A). Yet, they were significantly more coordinated with forward replay compared to reverse replay ($p = 0.0002$). Moreover, although other dMEC cells also showed weak coordination to both forward ($p = 0.0012$) and reverse ($p = 0.0055$) replay (Fig. 4B), they were not more coordinated with one type of replay over the other ($p = 0.59$). Indeed, the difference in replay coordination between the two dMEC cell groups was driven by the enhanced coordination that dMEC assembly cells showed for forward replay ($p < 0.0001$, Fig. 4C), whereas the difference in the degree of replay coordination between the two cell types did not differ for reverse replay ($p = 0.31$, Fig. 4D).

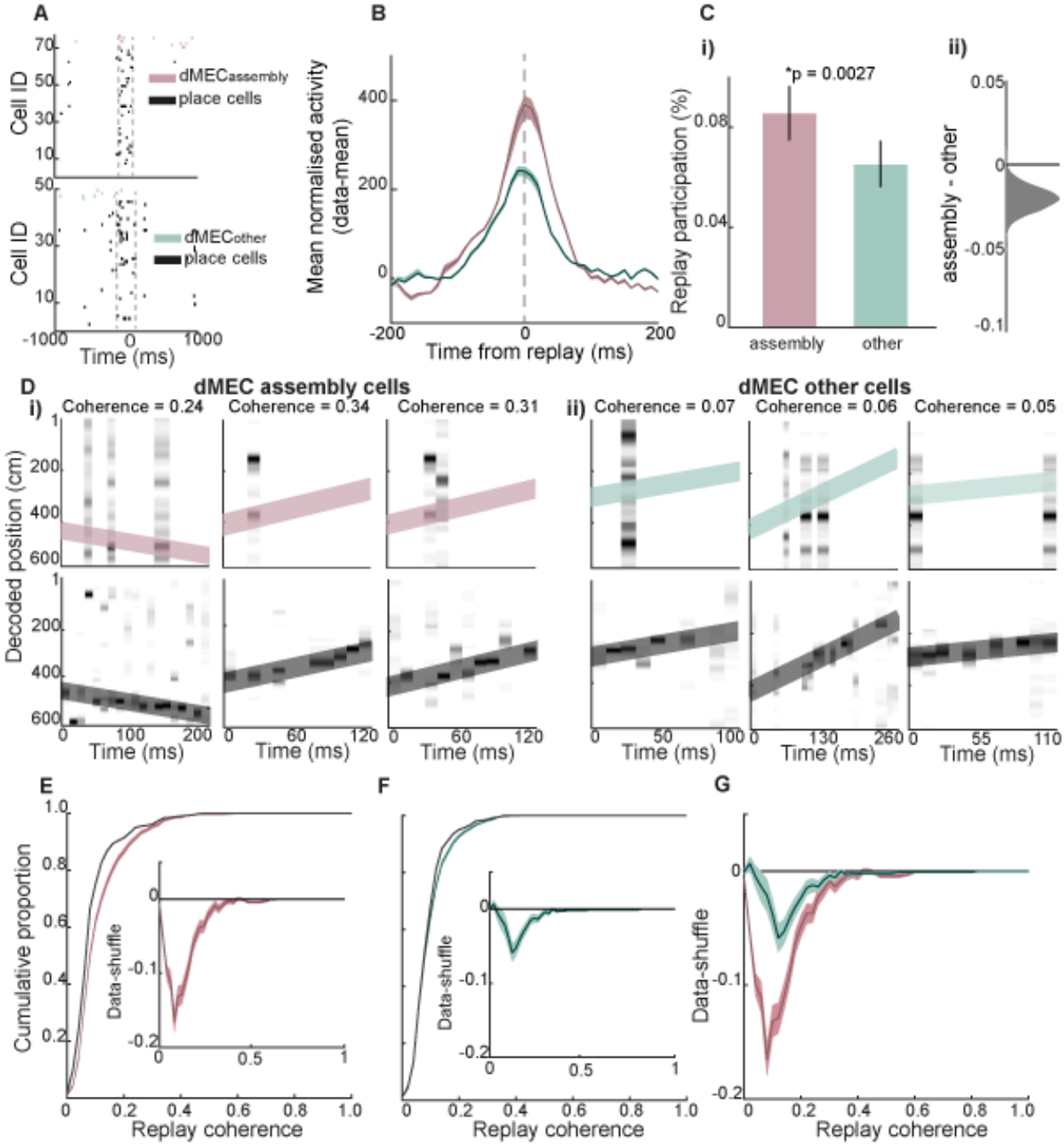

Figure 3. dMEC assembly cells participate in hippocampal replay. (**A**) Raster plot of two representative hippocampal replay events. Top: raster plot shows spikes from dMEC assembly cells (pink rasters). Hippocampal spikes are shown in black. Bottom: same as top panel but showing other dMEC cell spikes (green rasters). (**B**). Smoothed and mean normalised PSTH centred on hippocampal replay events for assembly and other dMEC cells. Shaded region shows

95% CI. (**C**) Left: Proportion of replay events dMEC assembly and other cells participate in, error bars show 95% CIs. Right: bootstrapped difference scores between assembly and other dMEC cells. (**D**). Representative replay trajectories with dMEC activity. (i) Bottom: position reconstruction based on CA1 spikes with best-fit line superimposed (dark grey diagonal line). Top: same as below but for dMEC assembly cells, CA1 best-fit line is fitted onto dMEC assembly decoding (pink diagonal line). Title shows dMEC-CA1 replay coherence. (ii) Same as (i) but for other dMEC cells. (**E**). Cumulative distribution of replay coherence scores for dMEC assembly cells, shaded area shows 1SD. Black line shows cumulative distribution of a cell ID shuffle. Inset: difference between the data and shuffle distribution. (**F**). Same as E but for other cells. (**G**) Data-shuffle distributions for the two dMEC cell types.

However, if dMEC cell coordination with hippocampal replay reflects entrainment to hippocampal assemblies then one would expect the replay coordination to be accentuated for events that specifically contain *both* members of a dMEC-CA1 assembly cell pair. To address this, we analysed separately replay events containing such assembly pairs (‘assembly events’) and those that only contained the dMEC assembly cell and other CA1 cells. First, we observed dMEC assembly cells were significantly more likely to be active in assembly events (11.81%, SD = 10.83) compared to non-assembly events (7.8%, SD = 7.35 $p = 0.0002$, Fig. 4E). However, assembly events showed similar functional coordination with replay compared to non-assembly events ($p = 0.075$, Fig. 4F). Yet, we observed replay coordination was significantly stronger for forward assembly events compared to forward non-assembly events ($p = 0.0042$, Fig. 4G). Whereas, for reverse replay events, replay coordination was similar for the two event types ($p = 0.81$, Fig. 4H).

Finally, if dMEC assembly cells play a privileged role in memory consolidation one might expect their coordination with replay to increase as the animals became more fluent with the task. To address this question, we analysed replay coordination for assembly and other dMEC cells as a function of how familiar the animals were with the Z-track. Specifically, we split the data into early (days1-2), mid (days3-4) and late (days5-6) learning periods. dMEC assembly cells displayed significant replay coordination during all learning periods (early: $p = 0.018$, mid: $p = 0.013$, late: $p < 0.0001$, Fig. 4Ii) and showed significantly greater coordination during late learning periods compared to early learning periods ($p = 0.0068$). To note, we observed a similar experience-dependent increase when the analysis was limited to assembly events (early vs mid: $p = 0.016$, early vs late: $p = 0.0021$, Fig. 4Ii). On the other hand, dMEC cells which did not display assembly-like activity showed no experience-dependent increase in replay coordination (all learning period comparisons $p > 0.05$, Fig. 4Ii). Moreover, we found the difference in replay coordination between the two cell types increased as the animals became more experienced with the task, reaching statistical significance during late learning periods (early: $p = 0.08$; mid: $p = 0.085$; late: $p < 0.001$, Fig. 4Iii).

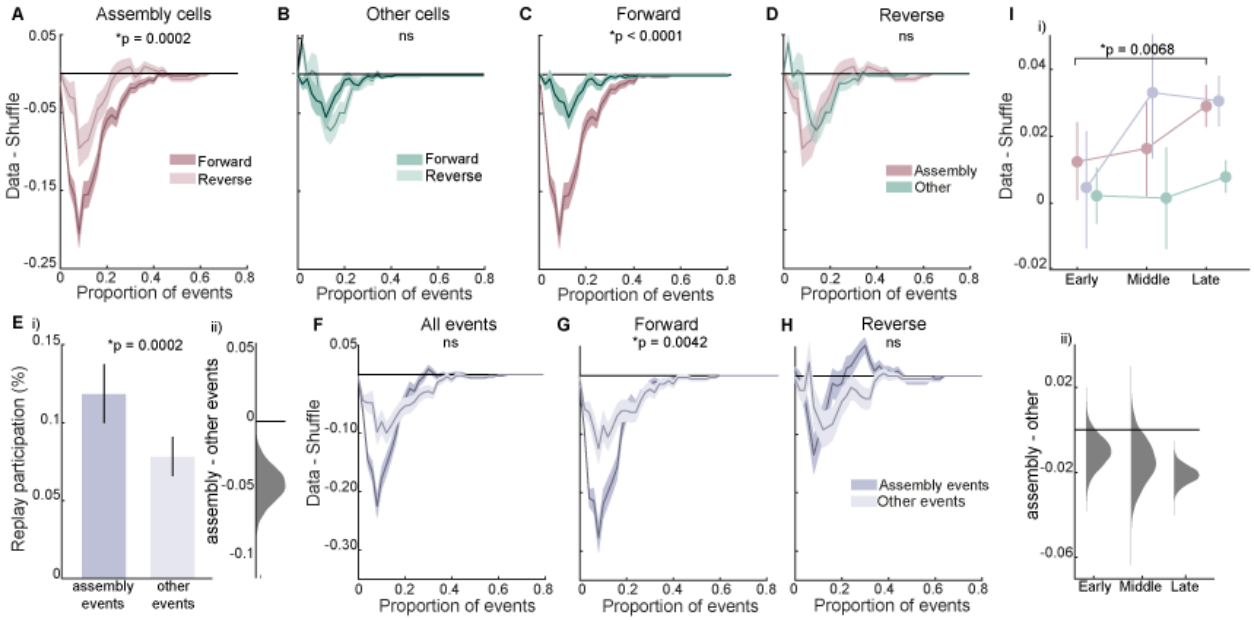

Figure 4. Participation of dMEC assembly cells in replay is modulated by the directionality of replay and learning. (**A**) Difference (y-axis) between data and shuffle cumulative distributions for dMEC assembly cell replay coherence (x-axis) separated by directionality of replay (dark = forward, light = reverse). (**B**) Same as A but for other dMEC cells. (**C**) Difference between data and shuffle cumulative distributions for forward replay coherence for assembly (pink) and other (green) dMEC cells. (**D**) Same as C but for reverse replay. (**E**) (i) Proportion of replay events dMEC assembly cells are active in separated by whether or not the event is an assembly event or not. (ii) Bootstrapped mean difference between assembly and non-assembly events. (**F**) Difference between data and shuffle cumulative distributions for dMEC assembly cell replay coherence. Distributions are plotted separately based on whether or not an event contained an assembly pair or not. (**G-H**) Same as F but for forward and reverse replay events, respectively. **I**) (i) Mean difference between data and shuffle replay coherence distributions for assembly and other dMEC cells as a function of experience with the track. (ii) Mean bootstrapped difference between assembly and other dMEC cells replay coherence across different levels of experience with the task.

Influential theories posit that the formation of long-term episodic and spatial memories relies on sub-second activity synchronisation between hippocampal and cortical units during offline periods(7, 23, 24). Yet it has hitherto remained unclear how slow, behavioural-time scale activity patterns during encoding can lead to millisecond-level cross-regional offline synchrony. We show this offline coordination may be mediated by the entrainment of cortical cells to hippocampal cell assemblies. Specifically, CA1 assembly-entrained dMEC cells were preferentially recruited to CA1 replay and expressed more similar locations during replay compared to other, non-entrained dMEC cells. Further, replay coordination of these dMEC assembly cells was heightened during

forward-projecting replay and when the replay included the dMEC cell's assembly partner. Finally, the assembly cell replay coordination showed a marked experience-dependent increase. We therefore conclude hippocampal-cortical replay coordination – a pre-requisite for memory consolidation – depends on the formation of hippocampal-cortical cell assemblies during encoding.

Cell assemblies have been mooted to perform a central role in synaptic plasticity and information propagation in neural circuits(14, 16). Namely, the ephemeral lifetime of cell assemblies fits the requirements for inducing spike-timing-dependent-plasticity(17) (STDP) and matches the membrane time constant (~10-30ms) of many principal cells(25). Thus, cell assemblies represent the ideal candidate for inducing plasticity in downstream circuits. Indeed, cell assemblies have been identified repeatedly in the hippocampus(14, 15) and their sequential expression - nested within individual theta cycles - is thought to be required for offline reactivations(26, 27). However, our study is the first to demonstrate hippocampal cell assemblies can entrain cortical neurons and that this entrainment may influence the establishment of hippocampal-cortical reactivation synchrony; a requirement for successful memory consolidation. Further, finding that a sub-population of cells residing in the deep-layers of the MEC may play a privileged role in memory consolidation is consistent with the anatomical position of this subregion – i.e. it is the principal output centre of the hippocampus(28, 29) - and extends emerging theories pointing to the dMEC as a critical sub-region supporting the effective transfer of memories to the cortex (30). Finally our findings highlight the central role of the theta rhythm in the propagation of information and neural synchronisation throughout the hippocampal-entorhinal system.

References

1. M. A. Wilson, B. L. McNaughton, Reactivation of hippocampal ensemble memories during sleep. Science 265, 676-679 (1994).

2. G. Girardeau, K. Benchenane, S. I. Wiener, G. Buzsaki, M. B. Zugaro, Selective suppression of hippocampal ripples impairs spatial memory. Nat Neurosci 12, 1222-1223 (2009).

3. H. F. Olafsdottir, D. Bush, C. Barry, The Role of Hippocampal Replay in Memory and Planning. Curr Biol 28, R37-R50 (2018).

4. I. Gridchyn, P. Schoenenberger, J. O'Neill, J. Csicsvari, Assembly-Specific Disruption of Hippocampal Replay Leads to Selective Memory Deficit. Neuron 106, 291-300 e296 (2020).

5. F. P. Battaglia, G. R. Sutherland, B. L. McNaughton, Hippocampal sharp wave bursts coincide with neocortical "up-state" transitions. Learn Mem 11, 697-704 (2004).

6. A. Sirota, J. Csicsvari, D. Buhl, G. Buzsaki, Communication between neocortex and hippocampus during sleep in rodents. Proc Natl Acad Sci U S A 100, 2065-2069 (2003).

7. H. F. Olafsdottir, F. Carpenter, C. Barry, Coordinated grid and place cell replay during rest. Nat Neurosci 19, 792-794 (2016).

8. H. F. Olafsdottir, F. Carpenter, C. Barry, Task Demands Predict a Dynamic Switch in the Content of Awake Hippocampal Replay. Neuron 96, 925-935 e926 (2017).

9. N. Maingret, G. Girardeau, R. Todorova, M. Goutierre, M. Zugaro, Hippocampo-cortical coupling mediates memory consolidation during sleep. Nat Neurosci 19, 959-964 (2016).

10. C. H. Vanderwolf, Hippocampal electrical activity and voluntary movement in the rat. Electroencephalogr Clin Neurophysiol 26, 407-418 (1969).

11. G. Buzsaki, E. I. Moser, Memory, navigation and theta rhythm in the hippocampal-entorhinal system. Nat Neurosci 16, 130-138 (2013).

12. M. E. Hasselmo, C. Bodelon, B. P. Wyble, A proposed function for hippocampal theta rhythm: separate phases of encoding and retrieval enhance reversal of prior learning. Neural Comput 14, 793-817 (2002).

13. N. Burgess, J. O'Keefe, Models of place and grid cell firing and theta rhythmicity. Curr Opin Neurobiol 21, 734-744 (2011).

14. K. D. Harris, J. Csicsvari, H. Hirase, G. Dragoi, G. Buzsaki, Organization of cell assemblies in the hippocampus. Nature 424, 552-556 (2003).

15. G. Dragoi, G. Buzsaki, Temporal encoding of place sequences by hippocampal cell assemblies. Neuron 50, 145-157 (2006).

16. G. Buzsaki, Neural syntax: cell assemblies, synapsembles, and readers. Neuron 68, 362-385 (2010).

17. G. Q. Bi, M. M. Poo, Synaptic modifications in cultured hippocampal neurons: dependence on spike timing, synaptic strength, and postsynaptic cell type. J Neurosci 18, 10464-10472 (1998).

18. T. Hafting, M. Fyhn, S. Molden, M. B. Moser, E. I. Moser, Microstructure of a spatial map in the entorhinal cortex. Nature 436, 801-806 (2005).

19. J. S. Taube, R. U. Muller, J. B. Ranck, Jr., Head-direction cells recorded from the postsubiculum in freely moving rats. II. Effects of environmental manipulations. J Neurosci 10, 436-447 (1990).

20. F. Sargolini et al., Conjunctive representation of position, direction, and velocity in entorhinal cortex. Science 312, 758-762 (2006).

21. T. Solstad, C. N. Boccara, E. Kropff, M.-B. Moser, E. I. Moser, Representation of Geometric Borders in the Entorhinal Cortex. Science. 322, 1865–1868 (2008).

22. W. E. Skaggs, B. L. McNaughton, K. L. Gothard, E. J. Markus, An Information-Theoretic Approach to deciphering the hippocampal code, in: Advances in Neural Information Processing Systems 5. eds. Hanson, S.J., Giles, C.L. & Cowan, J.D., pp. 1030–1037

23. D. Marr, Simple memory: a theory for archicortex. Philos Trans R Soc Lond B Biol Sci 262, 23-81 (1971).

24. G. Buzsaki, Two-stage model of memory trace formation: a role for "noisy" brain states. Neuroscience 31, 551-570 (1989).

25. C. Koch, M. Rapp, I. Segev, A brief history of time (constants). Cereb Cortex 6, 93-101 (1996).

26. C. Drieu, R. Todorova, M. Zugaro, Nested sequences of hippocampal assemblies during behavior support subsequent sleep replay. Science 362, 675-679 (2018).

27. L. Muessig, M. Lasek, I. Varsavsky, F. Cacucci, T. J. Wills, Coordinated Emergence of Hippocampal Replay and Theta Sequences during Post-natal Development. Current Biology. 29, 834-840.e4 (2019).

28. J. J. Chrobak, G. Buzsaki, Selective activation of deep layer (V-VI) retrohippocampal cortical neurons during hippocampal sharp waves in the behaving rat. J Neurosci 14, 6160-6170 (1994).

29. G. Surmeli et al., Molecularly Defined Circuitry Reveals Input-Output Segregation in Deep Layers of the Medial Entorhinal Cortex. Neuron 88, 1040-1053 (2015).

30. K. Z. Gerlei, C. M. Brown, G. Surmeli, M. F. Nolan, Deep entorhinal cortex: from circuit organization to spatial cognition and memory. Trends Neurosci, (2021).

Acknowledgments: We thank Daniel Bush and Federico Stella for useful feedback on the manuscript.

Funding: This work was supported by a Donders Mohrmann Fellowship to H.F.O. and a Sir Henry Dale fellowship to C.B..

Author contributions: H.F.O and C.B. conceived of the original experiment. H.F.O performed the original experiments and collected the original data. D.S.P. and H.F.O. conceived, designed and performed the analyses. D.S.P. and H.F.O. wrote the manuscript.

Competing interests: Authors declare that they have no competing interests.

Data and materials availability: Data analysis code (Python) used to analyses CA1-dMEC coupling is available on Gitlab(https://gitlab.com/diogo.santos.pata/theta-coordinates-hippocampal-entorhinal-ensembles-during-wake-and-rest), code for analysing replay (Matlab) can be obtained by contacting H.F.O. The raw data can be accessed here: https://doi.org/10.5281/zenodo.5566548

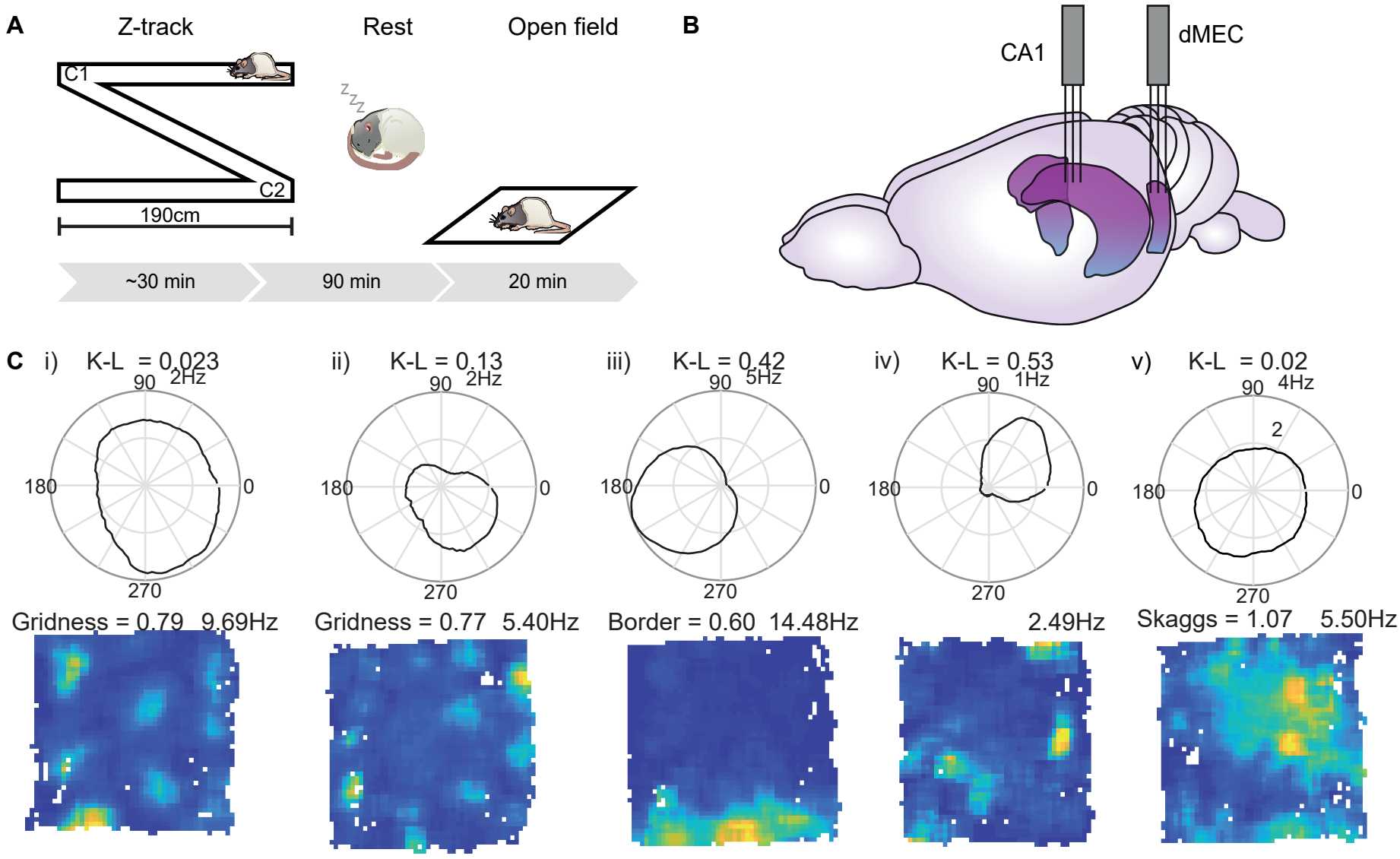
A
Z-track
Rest
Open field
C1
C2
190cm
~30 min
90 min
20 min
B
CA1
dMEC
C
i) K-L = 0.023
2Hz
Gridness = 0.79 9.69Hz
ii) K-L = 0.13
2Hz
Gridness = 0.77 5.40Hz
iii) K-L = 0.42
5Hz
Border = 0.60 14.48Hz
iv) K-L = 0.53
1Hz
2.49Hz
v) K-L = 0.02
4Hz
Skaggs = 1.07 5.50Hz
90
180
0
270

Figure1

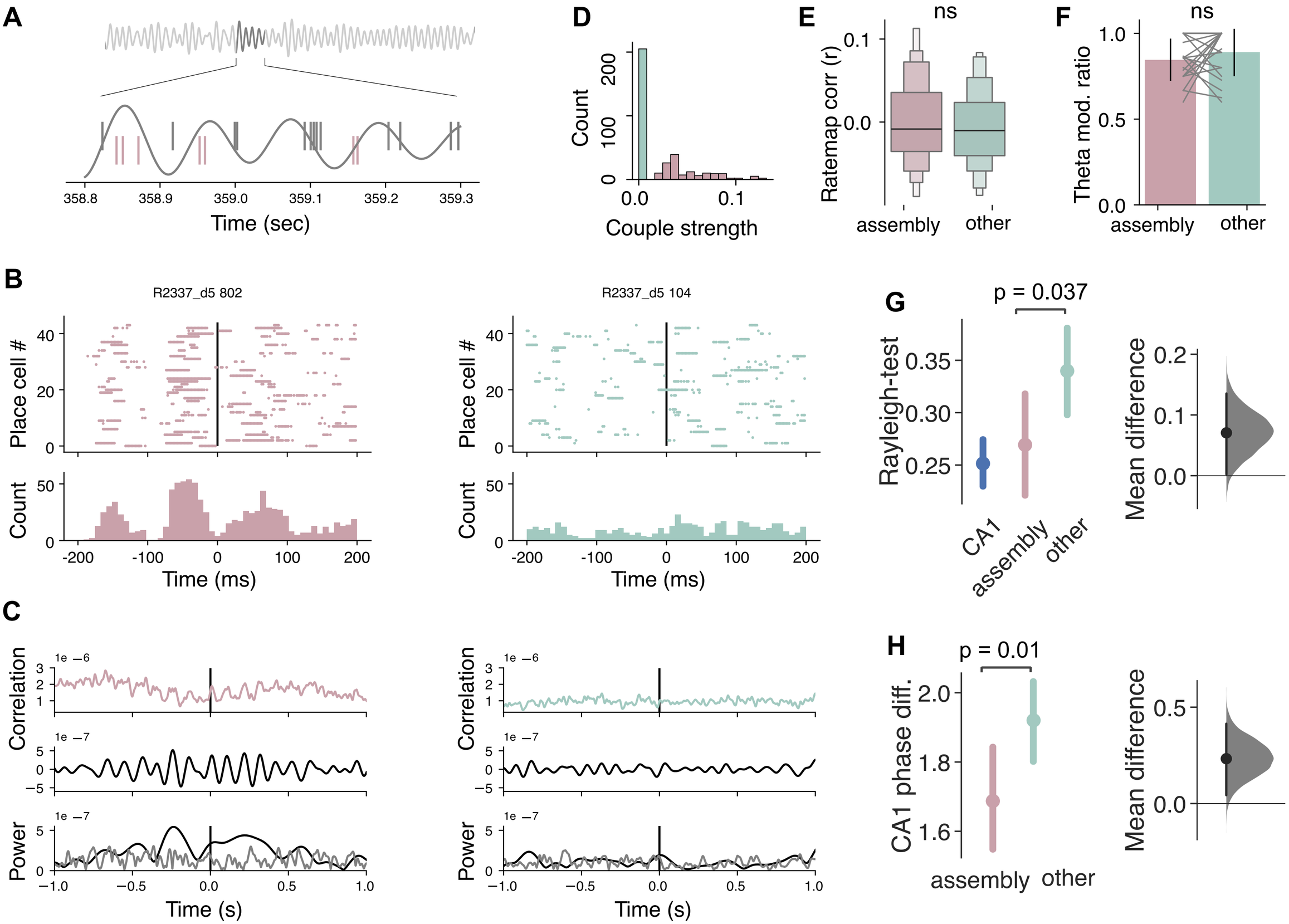
A
358.8
358.9
359.0
359.1
359.2
359.3
Time (sec)
D
Count
0
100
200
0.0
0.1
Couple strength
E
ns
Ratemap corr (r)
0.1
0.0
assembly
other
F
ns
Theta mod. ratio
1.0
0.5
0.0
assembly
other
B
R2337_d5 802
R2337_d5 104
Place cell #
40
20
0
Count
50
0
-200
-100
0
100
200
Time (ms)
C
Correlation
1e −6
3
2
1
1e −7
5
0
−5
Power
1e −7
5
0
−1.0
−0.5
0.0
0.5
1.0
Time (s)
G
p = 0.037
Rayleigh-test
0.35
0.30
0.25
CA1
assembly
other
Mean difference
0.2
0.1
0.0
H
p = 0.01
CA1 phase diff.
2.0
1.8
1.6
assembly
other
Mean difference
0.5
0.0

Figure 2

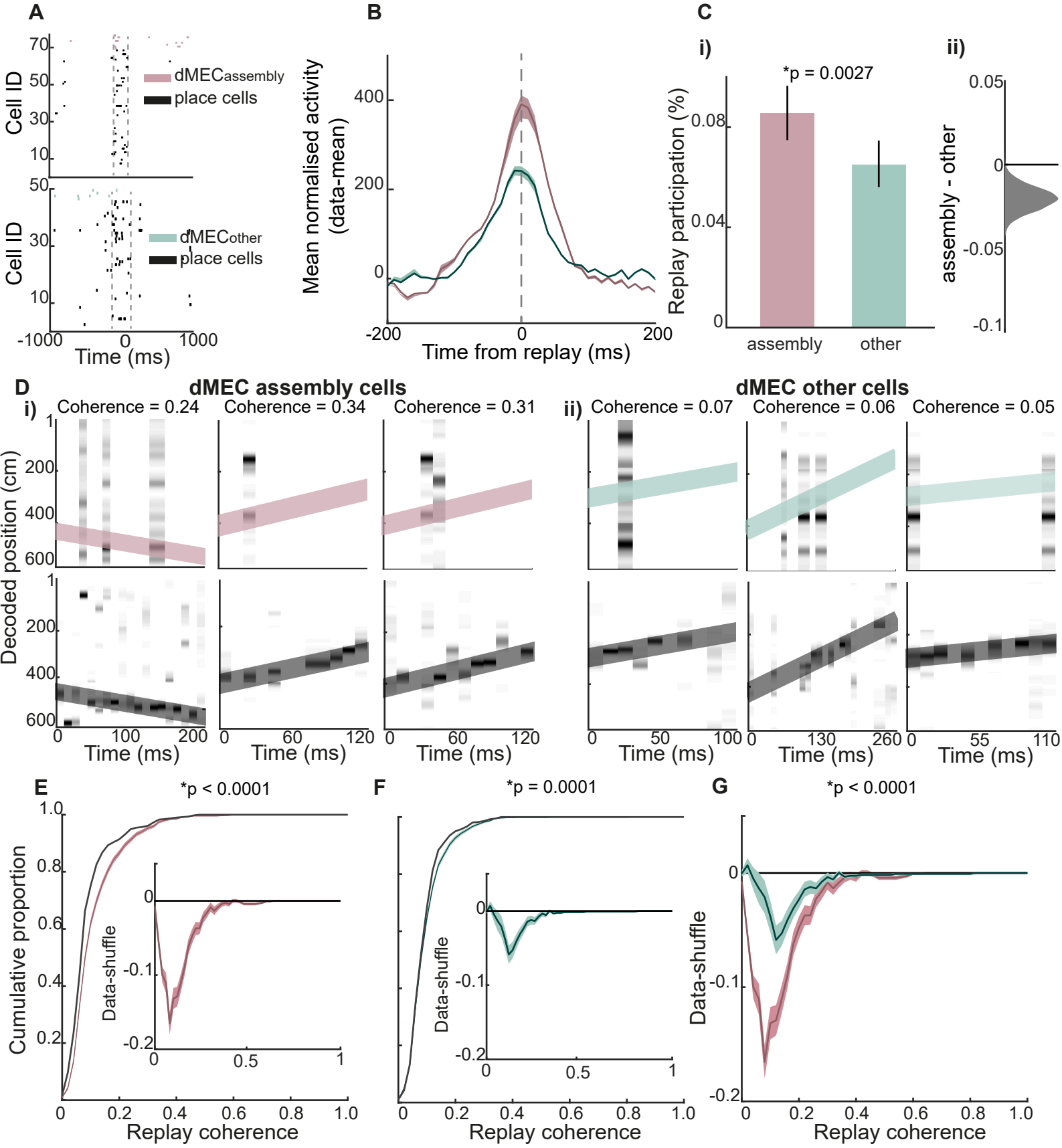
A
Cell ID
dMECassembly
place cells
dMECother
place cells
Time (ms)
B
Mean normalised activity (data-mean)
Time from replay (ms)
C
i)
*p = 0.0027
Replay participation (%)
assembly
other
ii)
assembly - other
D
dMEC assembly cells
dMEC other cells
i)
Coherence = 0.24
Coherence = 0.34
Coherence = 0.31
ii)
Coherence = 0.07
Coherence = 0.06
Coherence = 0.05
Decoded position (cm)
Time (ms)
E
*p < 0.0001
F
*p = 0.0001
G
*p < 0.0001
Cumulative proportion
Data-shuffle
Replay coherence

Figure 3

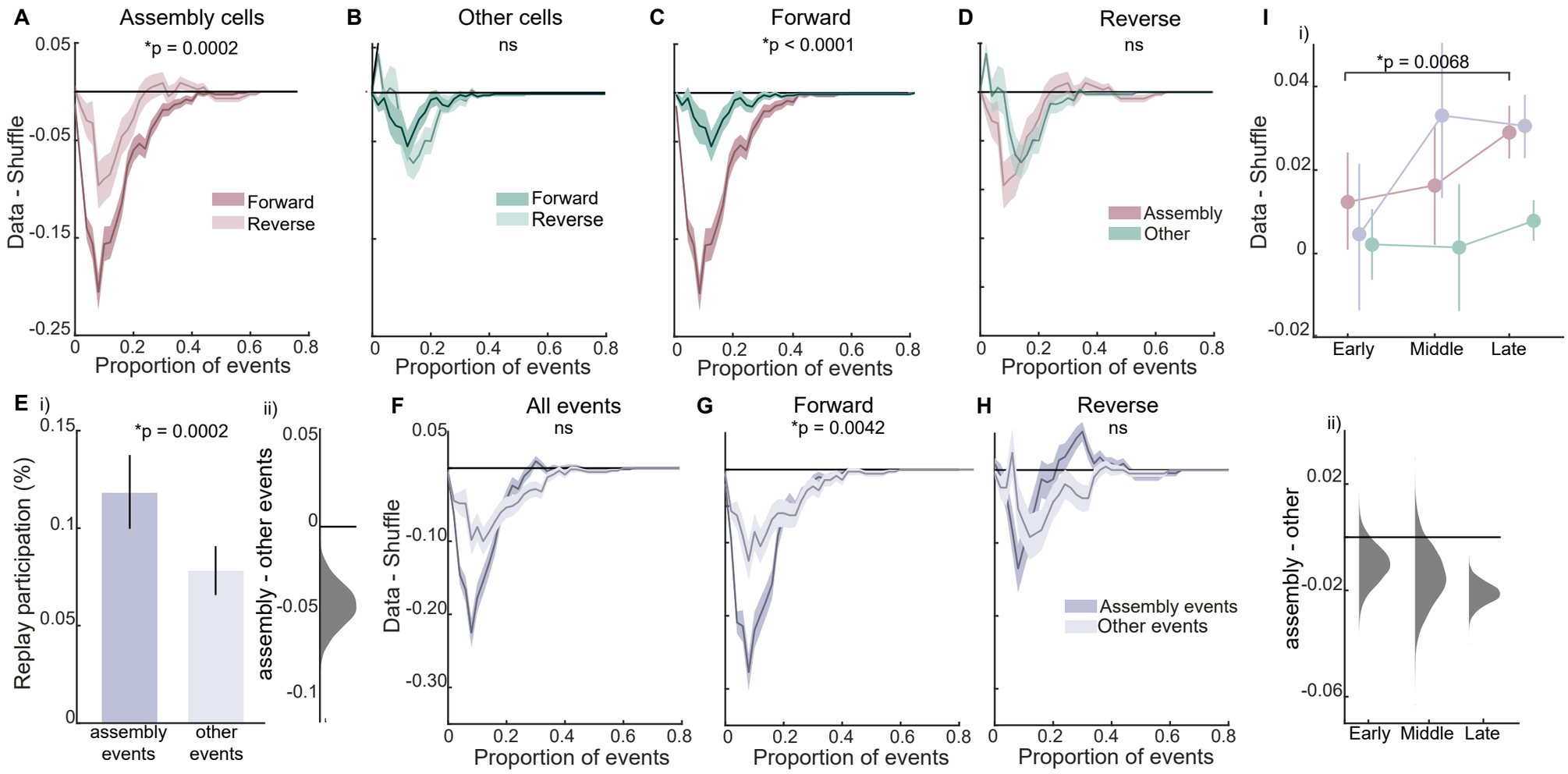
A
Assembly cells
*p = 0.0002
Data - Shuffle
Forward
Reverse
Proportion of events
B
Other cells
ns
Forward
Reverse
Proportion of events
C
Forward
*p < 0.0001
Proportion of events
D
Reverse
ns
Assembly
Other
Proportion of events
I
i)
*p = 0.0068
Data - Shuffle
Early
Middle
Late
E
i)
*p = 0.0002
Replay participation (%)
assembly events
other events
ii)
assembly - other events
F
All events
ns
Data - Shuffle
Proportion of events
G
Forward
*p = 0.0042
Proportion of events
H
Reverse
ns
Assembly events
Other events
Proportion of events
ii)
assembly - other
Early
Middle
Late

Figure 4

Supplementary Materials

Materials and Methods

Animals and surgery

Six male Lister Hooded rats were used in this study. All procedures were approved by the UK Home Office, subject to the restrictions and provisions contained in the Animals (Scientific Procedures) Act of 1986. All rats (330-400g at implantation) received two microdrives, each carrying eight tetrodes of twisted 17µm HM-L coated platinum iridium wire (90% and 10%, respectively; California Fine Wire), targeted to the right CA1 (ML: 2.2mm, AP: 3.8mm posterior to Bregma) and left medial entorhinal cortex (MEC) (ML = 4.5mm, AP = 0.3-0.7 anterior to the transverse sinus, angled between 8-10º). Wires were platinum plated to reduce impedance to 200-300kΩ at 1 kHz. After rats had recovered from surgery they were maintained at 90% of free-feeding weight with ad libitum access to water, and were housed individually on a 12-hr light/dark cycle.

Recording

Screening was performed post-surgically after a 1-week recovery period. An Axona recording system (Axona Ltd.) was used to acquire the single-units and positional data (for details of the recording system and basic recording protocol see Olafsdottir et al. (2016)). The position and head direction of the animals was inferred using an overhead video camera to record the location of two light-emitting diode (LED) mounted on the animals' head-stages (50Hz). Tetrodes were gradually advanced in 62.5um steps across days until place cells (CA1) or grid cells (MEC) were found.

Experimental apparatus and protocol

The experiment was run during the animals' light period to encourage quiet restfulness during the rest session. Animals ran on a Z-shaped track, elevated 75cm off the ground with 10cm wide runways. The two parallel tracks of the Z (190cm each) were connected by a diagonal section (220cm). The entire track was surrounded by plain black curtains with no distal cues. During each track session, animals were required to complete laps on the elevated Z-track, traversing each of the three tracks in order before returning in the other direction. At each end and corner, animals received a sweetened rice grain. Importantly, reward was withheld if the animal made an incorrect turn at the corners. Four animals (R2142, R2192, R2198, and R2217) were trained to run on the track for 3 days before recording commenced. For the other animals (R2242, R2335, R2336, R2337), recordings were made from the first day of exposure to the Z-track task.

Following the track session, rats were placed in the rest enclosure for 90 minutes. The rest enclosure consisted of a cylindrically shaped environment (18cm diameter, 61cm high) with a towel placed at the bottom and was located outside of the curtains which surrounded the Z-track. Animals were not able to see the surrounding room while in the rest enclosure. Prior to the experiment, rats had been familiarised with the rest enclosure for at least 7 days. Animals R2242, R2335, R2336 and R2337, were also placed in the rest enclosure for 90 minutes prior to the first Z-track session on day 1 of the experiment. Recordings from this 'pre-rest' session were not analysed as part of this study. Following the rest session, animals completed a 20min foraging session in an open field environment. This session was included to enable functional classification of MEC cells and was not analysed in the current study.

Data inclusion/exclusion

Sessions recorded on days1-6 were submitted for analysis. One session was excluded as result of data loss caused by the headstages becoming disconnected from the microdrives during the rest

session (R2336 day4) and one due to absence of an eeg recording (R2142, day4). In total 22 sessions were submitted for further analysis.

Data Analysis

Theta-band activity coupling

In order to assess theta-band activity coupling between dMEC-CA1 cell pairs, the densities of each cell spiking activity (1ms bins) during Z-track periods were extracted and lagged-correlated (-30 to 30 sec). The resulting and convolved (20ms) correlation vector was filtered in both the theta (5-12 Hz) and broad (20-125 Hz) bands (finite impulse response filter, 'Hamming' window), and then Hilbert-transformed to obtain their respective amplitude envelope (fig 2-C). Theta-broad band scores were then obtained by the theta and broad-band mean amplitude ratio within the -1 to 1 second window.

Next, we assessed whether each dMEC-CA1 cell pair was significantly coupled in the theta band by comparing the theta-broad band score against a distribution of spike time permutation derived theta-broad band scores (100 permutations). For each permutation, we randomly shifted the spike times of the dMEC cell (-2 to 2 seconds) and calculated the theta-broad band score. To control for multiple comparisons (i.e. the activity of each dMEC cell was compared to that of multiple CA1 cells) cells pairs whose theta-broad band score was above or equal the 99th percentile of the permutation distribution were considered to be coupled in the theta band

Theta coherence

dMEC cells were scored by their locking to ongoing hippocampal theta waves. To do so, we first identified the electrode in the CA1 region with strongest theta (5-12Hz) to delta (2-4 Hz) ratio. We filtered the selected CA1 channel's signal in the theta band (finite impulse response filter,

'Hamming' window), Hilbert-transformed it and extracted its instantaneous phase, allowing to identify the theta phase of each spike.

Only spikes elicited when the animal's running speed was above 3cm/s were included in this analysis. Theta coherence was computed via the Rayleigh test of uniformity on each cell's spiking theta phases.

Theta modulation

Theta modulation was computed for each dMEC cell individually. Similarly to theta-band activity coupling, each cell's spiking activity (1ms bins) density was computed, autocorrelated (-30 to 30 sec) and convolved (20 ms). Next, theta-band modulation score was calculated by comparing the strength of theta-band against the strength of broad-band as described for theta-band activity coupling. However, for theta modulation score, each permutation was performed by randomly scrambling spike times within the sessions time window. dMEC cells whose theta-band score was above or equal the 95 percentile of the permutation distribution were considered to be theta modulated.

Spike synchronization

Lagged spike synchronization between dMEC and CA1 cell pairs was quantified by computing the time difference between dMEC and CA1 spikes within the –200 to 200ms window aligned to dMEC spike times (Fig. 2B). The resulting spike-lag distribution (2ms bins) was normalised and smoothed (flat kernel size=20ms). Finally, we ran the same procedure 100 times but shifting the timings of dMEC spikes (-2 to 2 seconds) and used the 95 percentile of each time bin permutation distribution to assess significance .

Hippocampal replay

Ratemaps for the Z-track were generated after first excluding areas in which the animals regularly performed non-perambulatory behaviours (e.g. eating, grooming); the final 10cm at either end of the track and 5cm around each of the two corners. Similarly, periods when the animals' running speed was <3cm/s were also excluded. To generate ratemaps, the animals' paths were linearised, dwell time and spikes binned into 2cm bins and smoothed with a Gaussian kernel (σ = 5bins), firing rates were calculated for each bin by dividing spike number by dwell time. Separate ratemaps were generated for runs in the outbound and inbound directions. To identify place fields, spatial bins whose rate exceeded the mean firing rate of the cell on the track were only considered. Hippocampal cells were classified as place cells if they exhibited firing greater than its mean rate for 20contiguous bins and if the peak firing rate was >1hz. Interneurons, identified by narrow waveforms and high firing rates, were excluded from all analyses

Putative replay events were identified based on the activity of hippocampal place cells using a similar method to Olafsdottir et al(2016). To identify reactivation events, multi-unit (MU) activity from CA1 place cells were binned into 1ms temporal bins and smoothed with a Guassian kernel (σ = 5ms). Periods when the MU activity exceeded the mean rate by 3 standard deviations were identified as candidate reactivation events. The start and end points of each candidate event were determined as the time when the MU activity fell back to the mean. Events less than 40ms long were rejected.

For position decoding of reactivations a Bayesian framework(Olafsdottir et al., 2016) was used to calculate the probability of the animal's position in each spatial bin given the observed spikes; the posterior probability matrix. Note, two posterior probability matrices were generated for each event, one for inbound runs and one for outbound runs. Spike data was divided up into 10ms temporal bins, and decoding was carried out on each bin separately.

To score the extent to which putative trajectory events represented a constant speed trajectory along the linearised Z-track we applied a line-fitting algorithm(Olafsdottir et al., 2016). Lines were defined with a gradient (V) and intercept (c), equivalent to the velocity and starting location of the trajectory. The goodness of fit of a given line was defined as the proportion of the probability distribution that lay within 30cm of it. Specifically where P is the probability matrix:

$$R(V,c) = \frac{1}{n} \quad {}_{t=0}^{n-1} P(|x(t) - \ V.t.T + c) \ \leq d) \tag{1}$$

where t indexes the time bins of width and d is set to 30cm. was maximised using an exhaustive search to test all combinations of V between -50m/s and 50m/s in 0.5m/s increments (excluding slow trajectories with speeds > -2m/s and < 2m/s) and c between -15m and 21m in 0.01m increments.

To assess candidate replay events for significance we carried out a spatial field shuffle of the place cell ratemaps. Specifically, each ratemap was ‘rotated’ by shifting it relative to the track by a random number of bins drawn from a flat distribution between 1 and the length of the track minus 1 bin. The ratemap for each cell was rotated independently and in each case trailing bins were wrapped around to ensure an equal number of bins were used for each shuffle. This process was repeated 100 times for each event and for each shuffle we recalculated a goodness of fit measure (as described above). This enabled us to estimate the probability of obtaining a given event by chance. Replay trajectory events were defined as those with an individual p-value below 0.025 – to control for multiple comparisons for in- and outbound runs.

dMEC-hippocampal replay coordination

To analyse dMEC participation in replay events we carried out two analyses. First, the proportion of events a dMEC cell was active in was estimated for assembly and other dMEC cells. Second, a

peri-stimulus-time-histogram (PSTH) centred on the middle of a hippocampal replay event was generated for all candidate replay events. The PSTH was then summed and mean normalised (mean-data). To note, for replay participation analyses all candidate reactivation events were included (not just those expressing linear trajectories).

To investigate replay coordination between dMEC and place cells we applied the same framework as we did in previous work (Olafsdottir et al. (2016)). Namely, a bayesian decoding was done on dMEC cell spikes (to note, this analysis was done separately for assembly and other dMEC cells). Hence, for each replay event we also calculated a posterior probability matrix based solely on the observed dMEC cell spikes. Rather than fitting straight-line trajectories to the dMEC cell posteriors, we compared the best-fit line from the concurrently recorded place cell posterior. Specifically, the dMEC-place cell replay coherence score was calculated using the slope and intercept parameters of the best-fit line of the accompanying place cell event. This value we used to index replay coordination between hippocampal and dMEC cells. To estimate statistical significance of the observed coherence scores we used two different shuffling procedures.

In the first instance a shuffle distribution was generated by randomly permuting the cell IDs of dMEC cells so that cells were allocated a random ratemap (from other dMEC spatial cells recorded in the session). The line fitting procedure to estimate dMEC-place cell replay coherence, described above, was re-run. To assess the statistical significance of the obtained distribution of coherence scores against the shuffle we bootstrapped the data distribution 10,000 times, computing the cumulative distribution and the corresponding area-under-the-curve (AUC, i.e. the sum of the cumulative distribution) for each bootstrap. Difference scores between each of the 10,000 AUC scores obtained from the bootstrapped data and the shuffle distribution were computed and the 95% confidence interval estimated based on these difference scores. A result was deemed statistically significant if the confidence interval did not contain 0.

Second, we applied a spatial field shuffling procedure. This procedure was similar to the shuffling procedure used for place cell events. Specifically, each dMECcell ratemap was shuffled by shifting it relative to the track by a random number between 10 and the length of the track minus 10 bins. The ratemap for each cell was rotated independently and trailing bins were wrapped around to ensure an equal number of bins were used for each shuffle. This process was repeated 100 times for each event. For each shuffle, the dMEC-place cell replay coherence score was calculated using the slope and intercept parameters of the best-fit line of the accompanying place cell event (unshuffled). To assess statistical significance we used an AUC test as described above.

Experience-dependent analysis

To analyse change in dMEC-CA1 replay coordination as a function of experience with the task, the data was divided into three learning periods: early (days1-2), mid(days3-4) and late(days5-6). For each learning period the mean dMEC-CA1 replay coordination was calculated and subtracted from the mean obtained from the shuffle distribution for that learning period.

Functional classification of dMEC cells

dMEC cells were classified as grid cells using a shuffling procedure similar to that applied elsewhere. Specifically, the hexagonal regularity of each cell was assessed using the 'standard' gridness measure (Hafting, 2006). The values calculated for each cell were compared with a null distribution of 100 values obtained by calculating the gridness values of data in which the cell's spike train had been randomly permuted relative to the position of the animal by at least 30s. A cell was considered to be a grid cell and admitted to the main analysis if its standard or modified gridness value exceeded the 95th percentile of the matching null distribution.

Direction modulation was assessed by calculating the Kullback-Leibler (KL) divergence between the cell's polar rate map and a uniform circular distribution with equal mean:

$$D_{KL} = \sum_{i} \frac{\tau_1(i)\log(\tau_1(i))}{\tau_2(i)} \tag{2}$$

Where τ1(i) is the value in the ith bin of a polar rate map normalised to have area 1 (as a probability distribution) and τ2(i) is the ith bin of a uniform probability distribution with the same number of bins as τ1. Grid cells with KL divergence greater than 0.10 were considered to be directional.

Border score was computed as previously described (Solstad et al., 2008). In summary, each cell's firing fields were estimated by identifying groups of continuous spatial bins (bin size = 2cm) where the firing rate was above 30% of the cell's peak firing rate and smaller than 70% of the arena's area. Next, a border score (in the -1 to 1 range) was computed for each boundary individually by computing the relation between the firing field's extent and mean distance to the wall. As in Solstad et al. (2008), cells with a border score above 0.5 were considered border cells.

Spatial modulation was assessed using Skagg's information (Skaggs et al. 1993). Cells whose Skaggs information (bits/spike) exceed 1 were considered as spatial cells. To note spatial cells were those cells that were not classified as any of the other spatial cell types described above.

dMEC-CA1 field overlap

In order to account for potential confounds derived from similar spatial tunning between dMEC and CA1 cells, we quantified the overlap of each cell pair rate maps during Z-track for each running direction (in- and out-bound). Only spatial bins with positive rates were included. dMEC-CA1 field overlap was scored by computing the correlation coefficient (Pearson-R test) between the two cells rate maps.

Statistics

To compute statistical significance, all data were bootstrapped (resampling with replacement) and the 95% confidence intervals computed. For example, to assess if phase dMEC assembly cells were more likely to be active in replay events than other dMEC cells the distribution of replay participation scores were bootstrapped for assembly and other cells separately, and mean replay participation computed for each bootstrap. Then difference scores were computed by subtracting the bootstrapped replay participation scores of the dMEC assembly cells from the bootstrapped participation scores of other cells and the 95% confidence interval of this difference distribution computed. If the CI did not contain 0, the result was deemed statistically significant. To obtain p-values, the number of difference scores >0 was estimated and divided by the number of bootstraps (N= 10000).

Histology

Rats were anaesthetised (4% isoflurane and 4L/min O2), injected intra-peritoneal with an overdose of Euthatal (sodium pentobarbital) after which they were transcardially perfused with saline followed by a 4% paraformaldehyde solution (PFA). Brains were carefully removed and stored in PFA which was exchanged for a 4% PFA solution in PBS (phosphate buffered saline) with 20% sucrose 2-3 days prior to sectioning. Subsequently, 40-50μm frozen coronal sections were cut using a cryostat, mounted on gelatine-coated glass slides and stained with cresyl violet. Images of the sections were acquired using an Olympus microscope, Xli digital camera (XL Imaging Ltd.). Sections in which clear tracks from tetrode bundles could be seen were used to confirm CA1 recording locations.

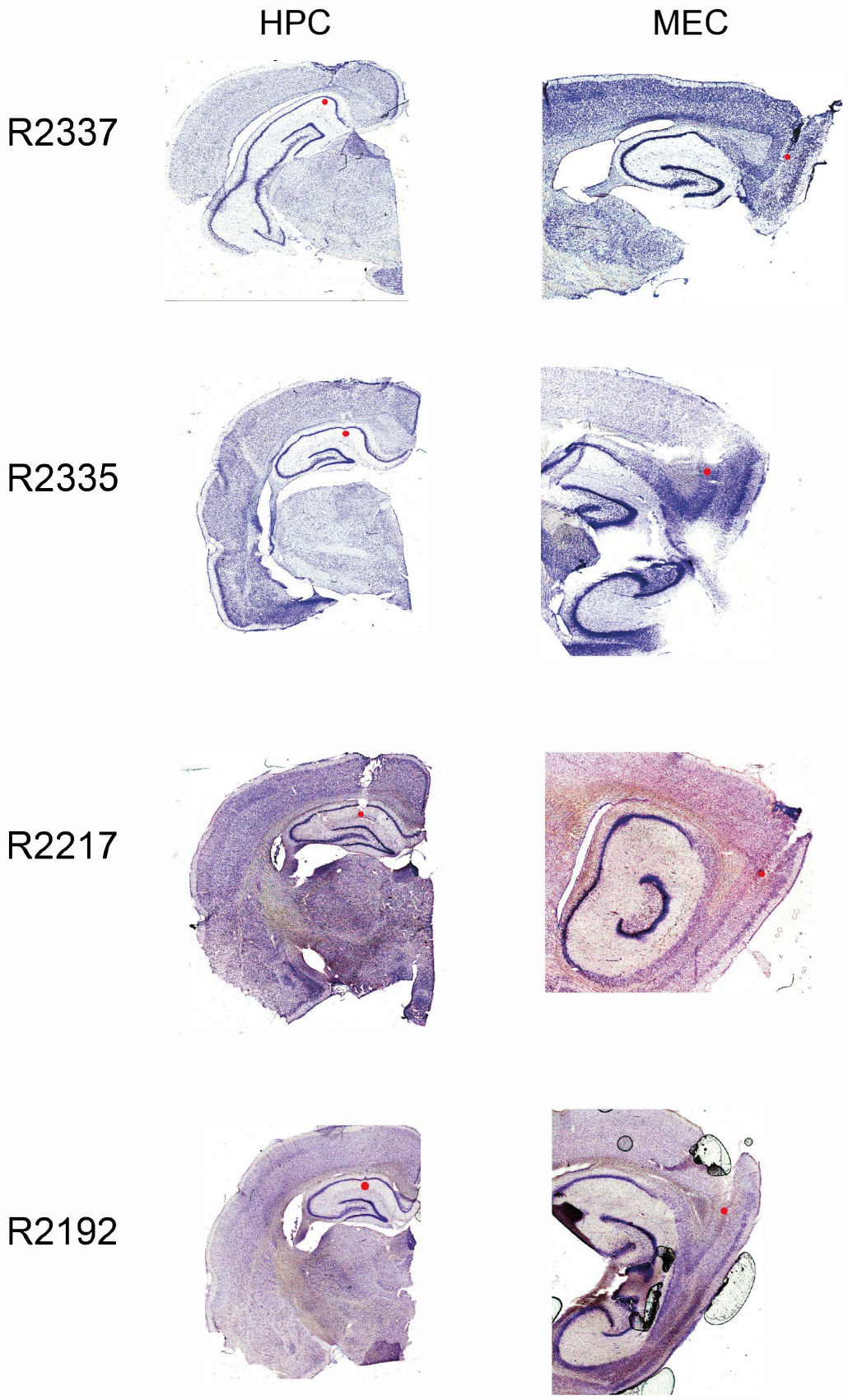

Figure S1. Tetrode locations. Four representative examples of Cresyl violet stained tetrode tracts from coronal (Hippocampus, left) and sagittal (MEC, right) sections. Red circle indicates the recording location for data included in this study. Left column shows rat ID.

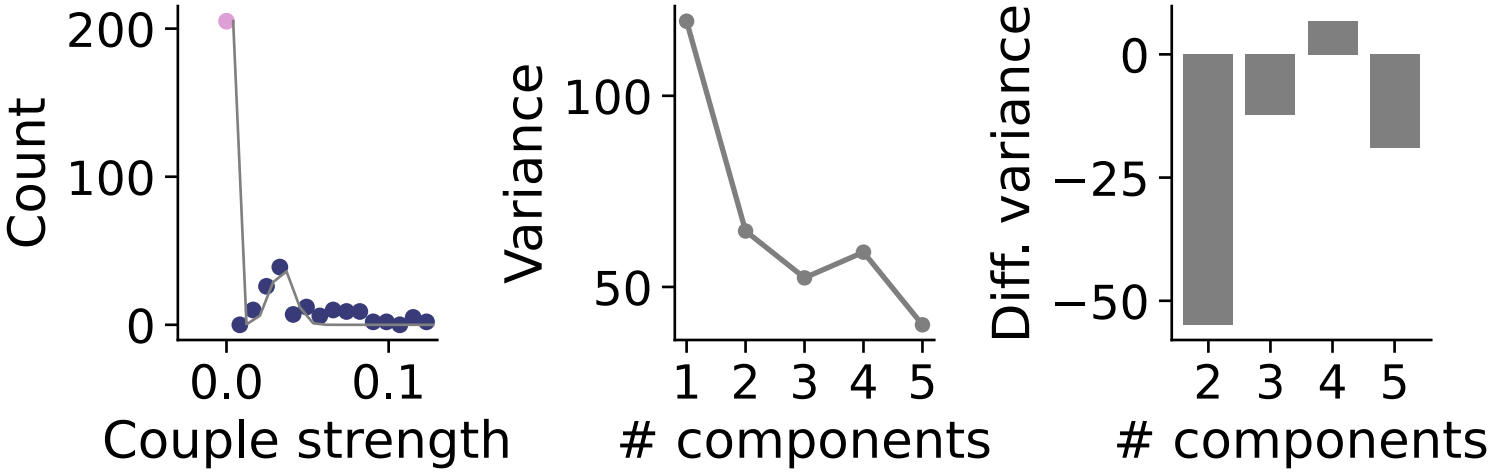

Figure S2. Bimodal distribution of dMEC thetaband couple strength to CA1 cells. Left: Distribution of cell count in function of a couple-strength was used to estimate the parameters of a Gaussian mixture model (python->sklearn/mixture/_gaussian_mixture). The resulting estimation allowed classification of cell type (other vs assembly cells, pink and blue dots respectively). A bimodal curve fitting procedure captured the two peaks of the distribution (grey line). Middle: Explained variance in function of the number of components chosen for each Gaussian mixture model. Right: The first derivative of the variance (in middle-plot) suggests that the model with 2 components (classes) has stronger gains in explaining the predicted variance.

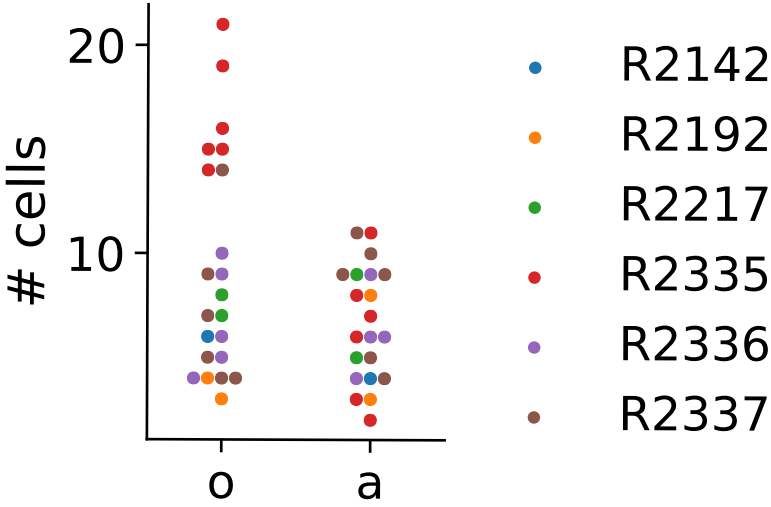

Figure S3. Number of assembly and other dMEC cells per session

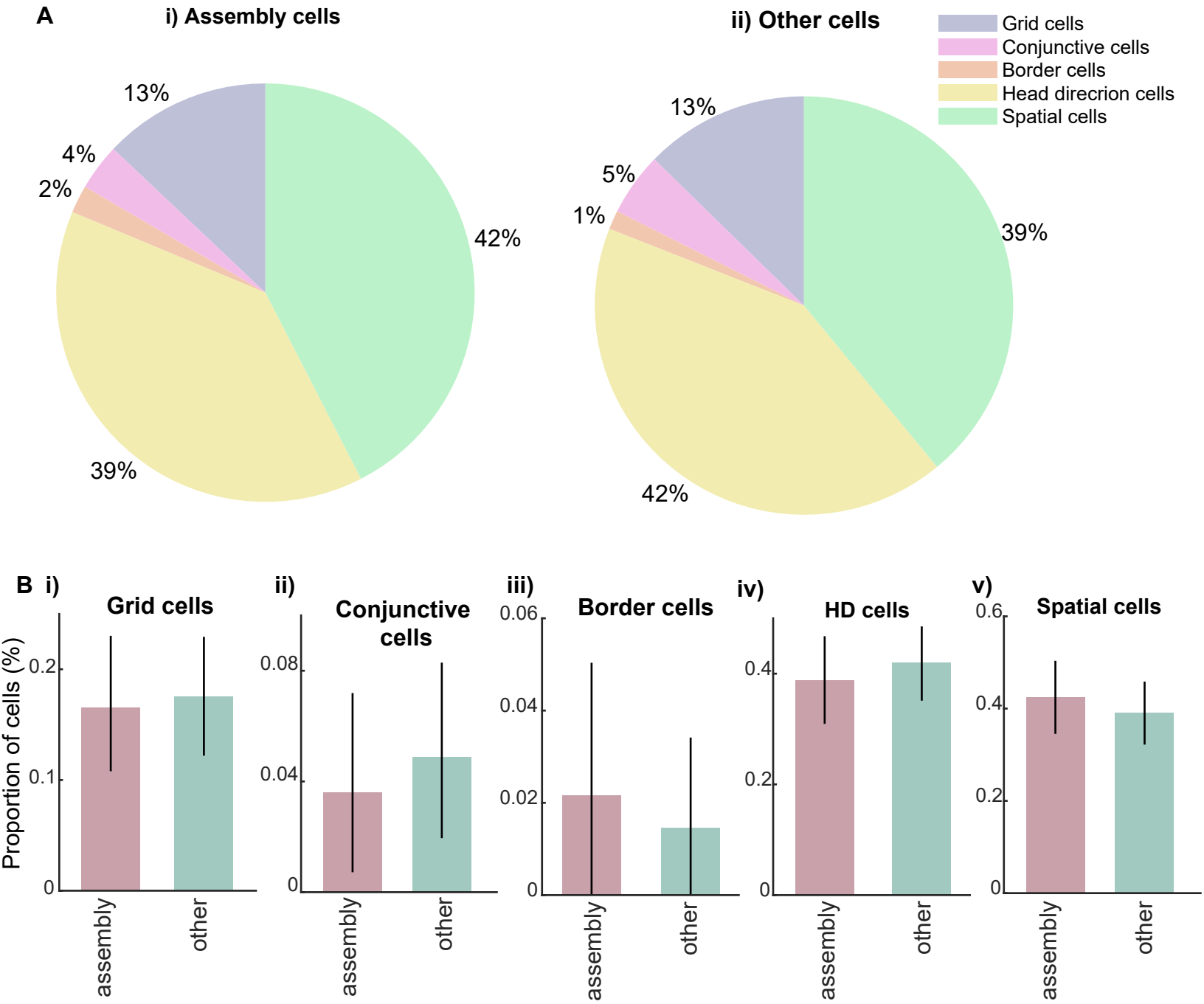

Figure S4. Functional classification of assembly and other dMEC cells. A Pie chart of spatial cell types in the assembly (i) and other (ii) dMEC cell group. **B** Proportion of different spatial cell types in the two dMEC cell subgroups.

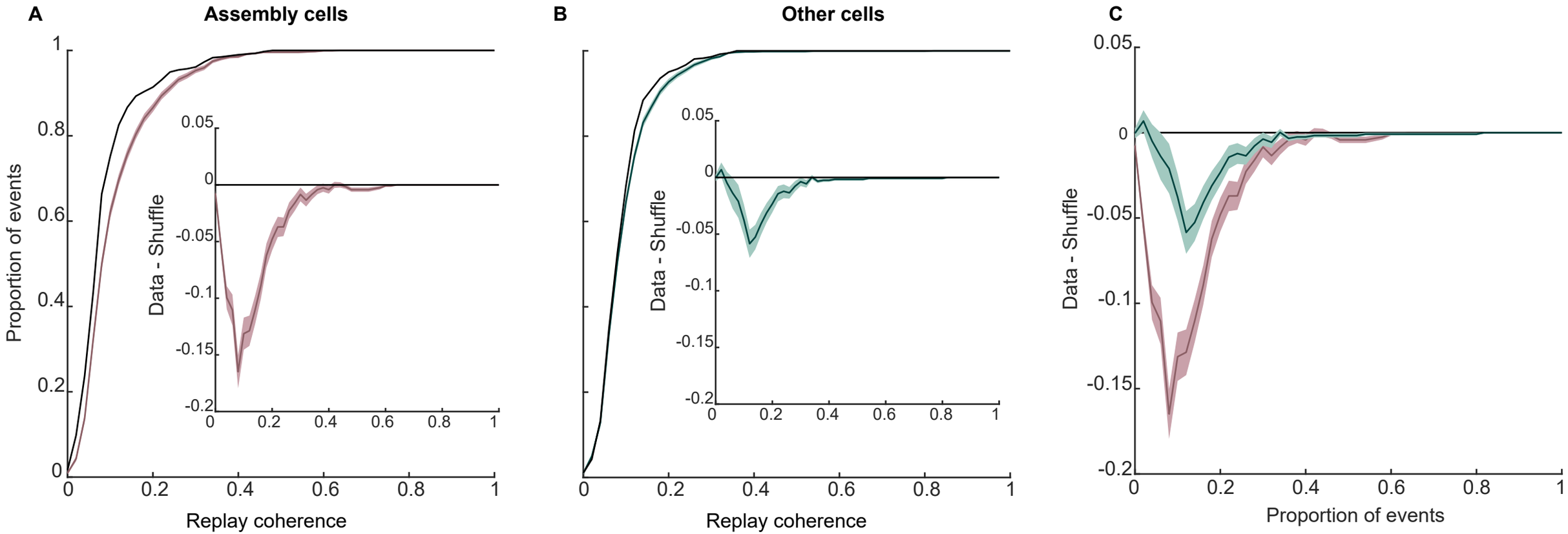

Figure S5. Replay coordination for assembly and dMEC cells using a spatial field shuffle. A Cumulative distribution of dMEC-CA1 replay coherence scores for dMEC assembly cells. Black line shows the chance distribution based on a spatial field shuffle. Inset: Difference between the data and shuffle distribution. **B** Same as A but for other dMEC cells. **C** Difference between the data and shuffle distributions for dMEC-CA1 replay coherence distributions for assembly and other cells.